

Balloon catheters with integrated stretchable electronics for electrical stimulation, ablation and blood flow monitoring



Lauren Klinker^a, Stephen Lee^a, John Work^a, John Wright^a, Yinji Ma^{b,c,d}, Leon Ptaszek^e, Richard C. Webb^f, Cliff Liu^a, Nirav Sheth^a, Moussa Mansour^e, John A. Rogers^f, Yonggang Huang^{c,d}, Hang Chen^{b,c,d,*}, Roozbeh Ghaffari^{a,*}

^a MC10 Inc., Cambridge, MA 02140, USA

^b Department of Engineering Mechanics and Center for Mechanics and Materials, Tsinghua University, Beijing 100084, China

^c Department of Mechanical Engineering, Center for Engineering and Health, and Skin Disease Research Center, Northwestern University, Evanston, IL 60208, USA

^d Department of Civil and Environmental Engineering, Center for Engineering and Health, and Skin Disease Research Center, Northwestern University, Evanston, IL 60208, USA

^e Massachusetts General Hospital, Harvard Medical School, Boston, MA 02114, USA

^f Department of Materials Science and Engineering, University of Illinois, Urbana, IL 60022, USA

ARTICLE INFO

Article history:

Received 17 January 2015

Received in revised form 22 February 2015

Accepted 22 February 2015

Available online 24 February 2015

Keywords:

Stretchable electronics

Balloon catheters

Ablation

Angioplasty

Hemodynamics

Mechanics

ABSTRACT

Balloon catheter-based techniques that apply mechanical force to blood vessel walls have dramatically advanced the standard of care for patients with vascular disease. But balloons are limited in their therapeutic potential because they rely on mechanics alone and lack electronically active materials. Recent advances in balloon catheters with integrated electrodes have offered additional treatment capabilities through the application of both mechanical contact force and radio frequency electromotive force. However, these smart balloons remain limited in their mechanics and their ability to provide diagnostic information about local vessel hemodynamics and tissue health near treatment zones. Here, we demonstrate a novel instrumented balloon catheter system that contains stretchable electrodes and thermal-based blood flow sensors, providing hemodynamic information, electrical stimulation, and ablation therapy on a single device. This system accommodates high inflation pressure (~ 2 atm) and twisting and bending over a broad range of vascular diameters and geometries. Finite element and analytical modeling capture the anisotropic mechanical and thermal properties of the device during cycles of inflation and deflation in a simulated biological environment. Bench-top ablation and *in vivo* blood flow measurements highlight the utility of this technology for clinical application.

© 2015 Elsevier Ltd. All rights reserved.

1. Introduction

Minimally invasive catheter-based devices have enabled both diagnostic and therapeutic advances in car-

diovascular and peripheral vascular interventions. With advances in balloon dilatation technologies and percutaneous transluminal coronary angioplasty (PTCA), balloon-based catheter systems have emerged as the standard of care for coronary artery disease, replacing coronary bypass surgical procedures [1]. PTCA gained even broader adoption with the introduction of bare metal and drug-eluting stents [2–4], which were found to provide additional protection against restenosis, while avoiding the risks asso-

* Corresponding authors.

E-mail addresses: chenhang.thu@gmail.com (H. Chen), rgghaffari@mc10inc.com (R. Ghaffari).

¹ Address: 9 Camp St., Cambridge, MA 02140, USA.

ciated with bypass surgery. Drug eluting balloons offered novel ways to locally deliver therapy (e.g. Paclitaxel) upon identification of plaque targets, as a way to mitigate risks of restenosis [5]. Although these smart balloon-based interventions reduce risks of restenosis, they lack diagnostic capabilities to assess the physicochemical properties and composition of the targeted arterial walls [1]. As a result, assessment of surrounding vessels that may be at risk for atherothrombotic injury [6] is difficult. Diagnostics that aim to assess the physicochemical properties and atherothrombotic risk of both the target and non-target vessels are desperately needed.

To address these diagnostic limitations, intravascular imaging techniques such as thermography, elastography, Raman spectroscopy and optical coherence tomography have provided additional methods for assessing the integrity and composition of vessel walls prior to PTCA [7,8]. While PTCA represents the standard of care in atherothrombotic disease, current technologies are limited in their ability to provide physiological information and intra-procedural feedback due to the lack of electronically active materials to interface with the endothelium. Recent advances in the development of semi-compliant and non-compliant balloons instrumented with surface-mounted electronics and biosensors offer additional capabilities in the diagnosis and treatment of vascular diseases [9]. In particular, balloon catheters with integrated conductive ribbons of silver and gold affixed on the outer balloon surface can be used to detect contact with vessel walls without fluoroscopy and to deliver radio frequency (RF) energy. AC electrical current ($\sim 300\text{--}500$ kHz) applied directly to biological tissue is often used therapeutically to ablate, stimulate or inhibit peripheral nerves [10] located deep within arterial walls. Although these devices have proven useful for some procedures, such as in renal sympathetic denervation, certain changes in local hemodynamics and vascular tone occurring during electrical stimulation remain poorly understood. Evaluation of these biological parameters requires additional instruments and increases procedure duration and complexity [9–17]. Moreover, the stiffness and limited compliance of conventional balloon-based electronics are not well matched to the soft, stretchable properties of biological tissue, thus giving rise to important safety concerns.

Here, we present a novel balloon-based catheter system that contains an integrated assembly of ablation, pacing, and blood flow sensors and actuators, thereby providing a means to assess vessel health, mechanical contact, and local hemodynamics intra-procedurally. Furthermore, the system is constructed on a compliant balloon substrate that, upon inflation, is readily expandable to fit a broad range of vessel anatomies and provide soft contact to the surrounding tissue. Finite element and analytical models highlight the ability of the balloon and electronics to expand and contract circumferentially and axially with minimal strain in the electronics and mechanical loading of the balloon substrate. These instrumented balloon catheters represent a major advance over existing angioplasty devices and are promising in their ability to reduce total duration and improve efficacy in routine vascular procedures, as evidenced by recent experimentation and preclinical studies.

2. Materials and methods

To develop stretchable electronics onboard balloon catheters, we first fabricated electrodes and flow sensors with designs that match the three-dimensional geometry of the stretchable balloon substrate [18–23]. Fig. 1(A) and (B) show the wavy geometry and locations of individual electrodes on the balloon surface and the placement of a flow sensor at the distal end of the circuit. The flow sensor consists of a thermistor and heating element that, when placed in the central lumen of a blood vessel, can continuously measure volumetric blood flow. Fig. 1(C) outlines the heterogeneous device stack used for the flow sensor and electrodes. Two layers of polyimide cover-layer (each ~ 10 μm thick) provide insulation and support for the copper/gold layer (~ 5 μm thick). The thickness of the metal layer is strategically designed to support both sensing and radio frequency stimulation. Standard photolithographic patterning was used to etch away the metal layers, while laser trimming was used to pattern the polyimide layers into wavy geometries.

2.1. Flow sensor design

The blood flow sensor measures flow by detecting changes in local temperature. Two thermistors are placed on the catheter: one at the distal tip of the catheter (Fig. 1(D), (E)) and a second on the catheter shaft proximal to the balloon (not shown). The proximal thermistor serves as a reference by measuring core body temperature in static blood and accounting for the effects of thermal drift caused by changes in body temperature. The difference between the proximal and distal sensors provides a drift-sensitive assessment of blood flow through the vessel lumen. A thermally conductive epoxy encapsulation (Fig. 1(D), in black) provides sufficient thermal conductivity to track changes in blood flow with low time constants. When coupled with a heating element, the distal thermistor continuously measures volumetric blood flow (Fig. 1(E)). The heating element, placed next to the distal thermistor, is used to maintain a constant temperature at the thermistor via a feedback loop. As blood flow increases and heat is drawn from the distal thermistor, the power to the heating element will increase in order to maintain a given temperature at the distal thermistor. A proportional–integral–derivative (PID) controller is used to maintain the constant temperature feedback loop and increase the power delivered to the heating element. Similarly, when blood flow decreases, the PID controller reduces power to the heating element and allows the distal thermistor to cool (Fig. 1(E)). Additional computational techniques, such as ω and 3ω , may be used to obtain a better signal-to-noise ratio and improve filtering.

2.2. Flow sensor data acquisition software

The flow sensing software performs three primary functions: (i) control of the feedback loop to maintain a steady constant set point temperature difference between the two thermistors; (ii) data display in real time; (iii) logging of data during catheter insertion, measurement, and removal.

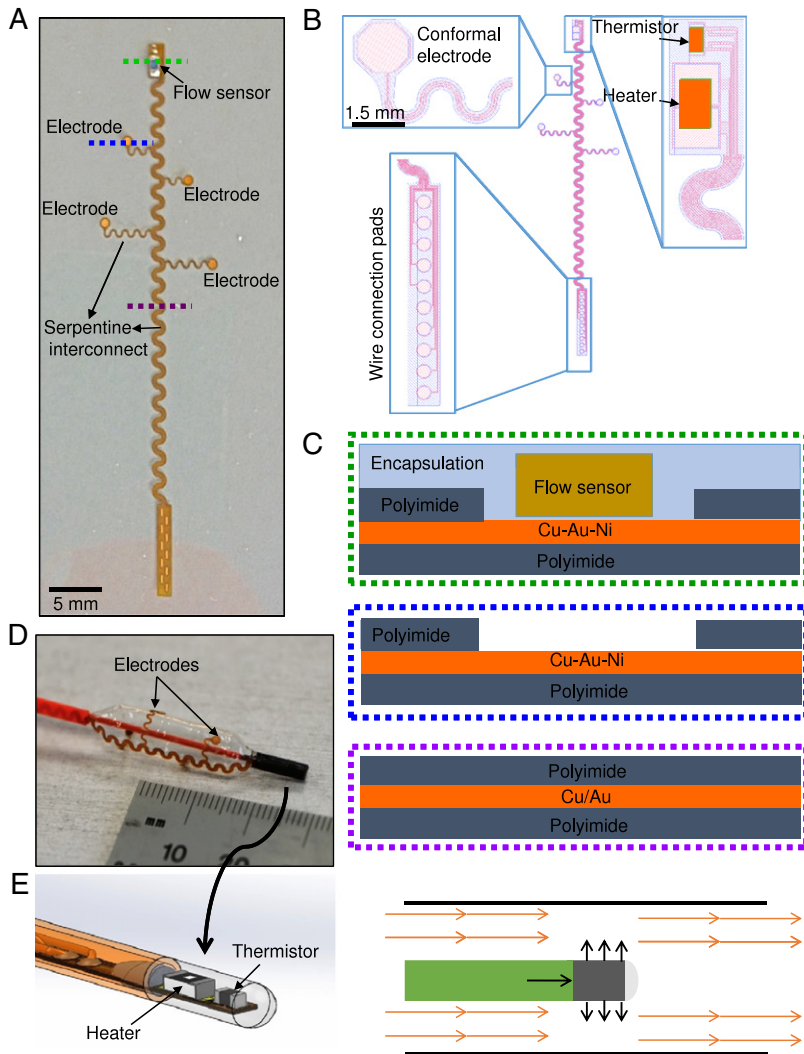


Fig. 1. Fabrication of balloon integrated electronics. (A) Optical image of stretchable, interconnected array of electrodes, flow sensor, and contact pads in a 2-dimensional planar configuration. (B) Schematic drawing of conformal electrodes, serpentine geometry, connection pads and location of the flow sensor sub-components (i.e. thermistor and heater). (C) Cross-sectional drawing of stretchable electronics stack near the electrodes, flow sensor and metal interconnects. (D) Optical image of 3-dimensional balloon catheter with integrated electrodes and flow sensors. (E) Exploded drawing of flow sensor near the tip of the balloon catheter. (Right panel) Conceptual drawing of blood flow (orange arrows) in a vessel and changes in thermal flux (black arrows) captured around flow sensor.

In addition to thermal measurements, the software also logs data from an external optical pressure sensor. The data from the flow sensing and pressure sensing modalities are then used to calculate cardiovascular resistance. All calculations require a multi-order curve fit to convert the measured voltage into a blood velocity, which can be converted to a volumetric flow rate (mL/min) if the diameter of the vessel is known.

The system has been thoroughly tested in a bench-top flow system as well as in a number of preclinical studies in porcine models. Upon insertion of the catheter into a vascular lumen, the system is able to respond quickly and deliver hemodynamic data within seconds. With the use of a reference thermistor, this flow data also accounts for intra-procedural changes in core body temperature that are routinely observed and would otherwise compromise

measurement validity. Altogether, this system is able to provide valuable physiological information without disrupting the clinical workflow during standard vascular procedures.

2.3. Flow sensor data acquisition hardware

The hardware provides a programmable excitation using a current source (up to 50 mA at ± 10 V) from 1 to 100 kHz to the heating element. Another programmable excitation provides current (up to 500 μ A at ± 10 V) from 1 to 100 kHz to both the distal thermistor and the reference thermistor. The two thermistors are placed in series, with the same electrical current driving both components. Each of the two thermistors is measured differentially and their voltages are subtracted from one another. As part of the

feedback loop, physiologically induced changes in blood flow will cause the heating element to modulate its current in order to maintain a constant temperature at the distal thermistor.

The system is galvanically isolated to 5 kV. The hardware design indicates excessive current and can disable the current to the device in such an event. Lastly, grounding is arranged such that all current is accounted for and, if leakage is detected, the console can disconnect from the catheter.

2.4. Flow sensor user interface

The data acquisition console has a built-in display to continuously monitor blood velocity (in cm/s), blood flow rate (in mL/min), and cardiovascular resistance (pressure/flow, in mm Hg per mL/min). The console consistently displays instantaneous flow rates at scrollable time points, as well as sensor diagnostic information, such as the thermistor and heater voltages. The graphical user interface can also lead the operator through a procedure-specific sequence of events, such as catheter insertion, pre-ablation or pre-stimulation measurements, post-ablation or post-stimulation measurements, and catheter removal. All data is time stamped and logged continuously over the course of the entire procedure. The control software is designed such that it can be set to specific parameters for stimulation and/or tissue ablation. Although it is not automated, the ablation module could apply ablation at set times following hemodynamic measurements.

2.5. Bench top flow experiments

Experiments employing a bench top flow apparatus consisting of a perfusion chamber with a tunable infusion pump were performed. Deionized water and heparinized blood were equilibrated at body temperature ($\sim 37^\circ\text{C}$) using an external heating device. The apparatus was then perfused using an infusion pump. The effects of fluid viscosity and temperature on the flow sensor response were systematically tested over volumetric flow rates within a biological range (0–500 mL/min). These experiments served to define the relationship between sensor voltage and flow rate for *in vivo* studies.

2.6. Animal experiments

All experimental protocols were reviewed and approved by the AccellLAB Institutional Animal Care and Use Committee in accordance with the Canadian Council on Animal Care. Farm swine were sedated with an intramuscular injection of ketamine (25 mg/kg), azaperone (4.0 mg/kg), and atropine (0.04 mg/kg) followed by intravenous administration of propofol (1.66 mg/kg). Intubation was achieved with a 7.5 mm endotracheal tube and supported by mechanical ventilation at 10–15 breaths/min. A surgical plane of anesthesia was maintained throughout the procedure with 1%–2% isoflurane and oxygen. Access sites near the femoral artery were cleaned with topical chlorohexidine, 70% isopropyl alcohol, and povidone iodine. This area was draped to maintain a sterile field and

access was gained at the femoral arteries and at the left femoral vein via inguinal skin incisions. Arterial sheaths (Flexor, Cook Medical Inc., Bloomington, IN) were introduced and advanced into each of the femoral arteries. The catheter was deployed in the femoral artery and measurements were performed within the peripheral and central vasculature, including the renal arteries, abdominal aorta, and coronary arteries.

3. Results and discussion

3.1. Mechanical properties of integrated electronics on balloon

Fig. 2(A)–(C) show images of an angioplasty balloon catheter consisting of a passive array of electrodes, a long serpentine interconnect along the axial direction and several short serpentine interconnects that span along the circumferential direction. The balloon and integrated electronics experience deflation (i.e., vacuum inside the balloon; Fig. 2(A)), normal inflation pressure (i.e., ~ 1 atm for both inside and outside the balloon; Fig. 2(B)), and high inflation pressure (i.e., ~ 2 atm inside the balloon, Fig. 2(C)). The mechanical behaviors of the inflated and deflated balloon states are predicted with finite element analysis (FEA; Abaqus [24]) (Fig. 2(D)–(F)). In Fig. 2(E), FEA shows maximum strains are much less than 0.1% in corresponding to normal inflation pressure. The electrodes are strategically located near the cylindrical part of the balloon, away from the distal and proximal ends, allowing direct contact with vessel walls during inflation. The bending stiffness of the serpentine interconnects (3.55×10^{-5} N m) for a stack consisting of 5 μm -thick Au sandwiched between two 25 μm -thick PI is two orders of magnitude larger than that of the balloon (3.33×10^{-7} N m for unit width of 50 μm -thick polyurethane with Young's modulus of 32 MPa [25]). As a result, the bending curvature of serpentine interconnect is very small. Nevertheless, the electronics are robust and can support high current densities in this configuration. For balloons in their deflated state (Fig. 2(A) and (D)), the maximum strain in the metal layer approaches $\sim 0.7\%$ near the junctions between axial and circumferential serpentines due to decreased local curvature. In the extreme inflation state (Fig. 3(C) and (F)), the maximum strain in the metal layer approaches $\sim 9.0\%$ in the circumferential serpentine interconnects, which is slightly lower than the fracture strain for gold ($\sim 10\%$) [26]. The serpentine interconnects are thus primarily stretched during high inflation state and behave like springs, whereas in-plane bending-dominated deformations occur during deflation. In fact, the effective tensile stiffness of the circumferential serpentines (5242 N/m per unit width, where serpentines interconnect is modeled as semi-circle beam with radius 0.43 mm and width 0.3 mm) is just within a factor of 3 of the tensile stiffness of the balloon (1600 N/m per unit width; 50 μm -thick polyurethane with Young's modulus ~ 32 MPa [25]). On the contrary, the strains in the circumferentially branching electrodes are small ($< 0.1\%$) during both deflation and high inflation pressure cycles because its tensile stiffness (4.2×10^5 N/m for 5 μm -thick Au and 10 μm -thick PI given by FEA) is much greater than that of the balloon

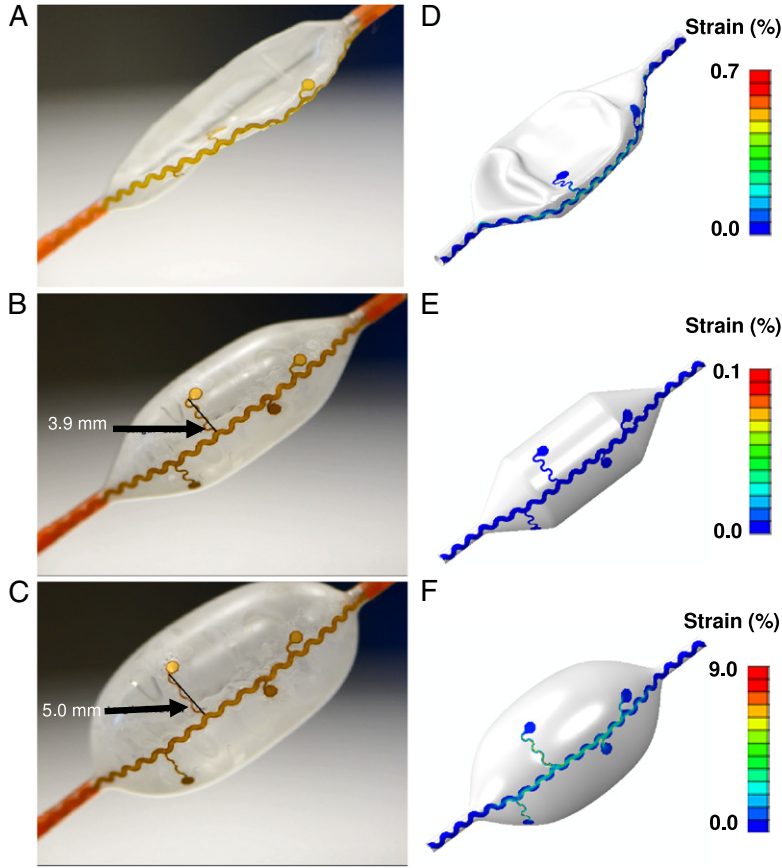


Fig. 2. Balloon mechanics during deflation and inflation cycles. Optical image of stretchable balloon with integrated electrodes in deflated (A), inflated (B) and stretched (C) states. FEA results show the strain distribution color map for deflated (D), inflated (E) and stretched (F) states. The legend in the right panel highlights the strain levels for each state of inflation/deflation. (For interpretation of the references to color in this figure legend, the reader is referred to the web version of this article.)

(1600 N/m). We thus locate these electrodes in regions that allow proper mechanical flexibility and allow circumferential sensing/ablation (Fig. 2(A)) during clinical operation.

Fig. 3 illustrates the finite-deformation mechanics model for the inflated balloon. We focused our analysis on the cylindrical region of the balloon, which is substantially longer than the distal and proximal regions that are affixed to the catheter extrusion (Fig. 2(B)). As shown in Fig. 3(A), h , l and r denote the thickness, length and radius of the cylindrical part of the balloon, respectively. First we consider the bare balloon, without integrated electronics. The stress increments exerted in the axial and circumferential directions due to incremental pressure differences dp at equilibrium are given by:

$$\begin{cases} d\sigma_{\text{axial}} = \frac{r}{2h} dp \\ d\sigma_{\text{circumferential}} = \frac{r}{h} dp. \end{cases} \quad (1)$$

The incremental stress dp is negligible compared to $d\sigma_{\text{axial}}$ and $d\sigma_{\text{circumferential}}$ for the balloon thicknesses ($h \sim 50 \mu\text{m}$) much smaller than the radius r ($\sim 10 \text{ cm}$). The incremental logarithmic strains are then obtained using Young's modulus E ($=32 \text{ MPa}$) and Poisson's ratio ν ($=0.32$) as expressed

by:

$$\begin{cases} \frac{dh}{h} = d\varepsilon_{\text{radial}} = \frac{-\nu}{E} (d\sigma_{\text{circumferential}} + d\sigma_{\text{axial}}) \\ = \frac{-3\nu r}{2Eh} dp \\ \frac{dr}{r} = d\varepsilon_{\text{circumferential}} = \frac{1}{E} (d\sigma_{\text{circumferential}} - \nu d\sigma_{\text{axial}}) \\ = \left(1 - \frac{\nu}{2}\right) \frac{r}{Eh} dp \\ \frac{dl}{l} = d\varepsilon_{\text{axial}} = \frac{1}{E} (d\sigma_{\text{axial}} - \nu d\sigma_{\text{circumferential}}) \\ = \left(\frac{1}{2} - \nu\right) \frac{r}{Eh} dp. \end{cases} \quad (2)$$

It is noted that Eq. (2) is in differential form, which involves true stress and strain increments, so that it can account for the balloon's large and nonlinear deformation as the constitutive relation keeps linear elastic for large deformation. The ratio of the first and second equations in Eq. (2) yields $dh/h = -3\nu dr / [(2 - \nu)r]$, which is then integrated to give $h/h_0 = (r/r_0)^{-3\nu/(2-\nu)}$, where $h_0 = 50 \mu\text{m}$ denotes the initial thickness for $p = 0$. Substituting the above relation into the second equation in Eq. (2) gives an expression

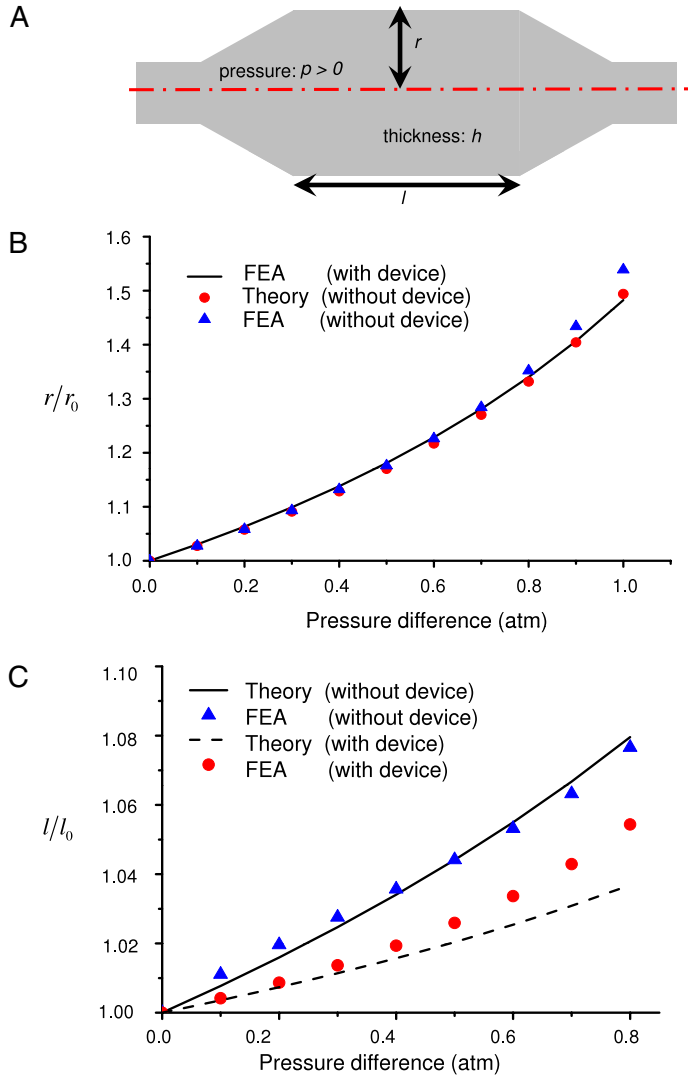


Fig. 3. FEA and analytical modeling of axial and circumferential strains. (A) Conceptual drawing of important parameters used to characterize circumferential and axial strain distributions. (B) Theoretical predictions (FEA and analytical solutions) of circumferential strain–stress relationship for balloon catheter with and without integrated stretchable electronics. (C) Theoretical predictions (FEA and analytical solutions) of axial strain–stress relationship for balloon catheter with and without integrated stretchable electronics. The mechanical loading by the stretchable electronics yields different strain–stress curves compared to balloon strain profile without electronics.

for the radius r of the balloon:

$$\frac{r}{r_0} = \left[1 - \frac{(1 + \nu) r_0}{Eh_0} p \right]^{\frac{-(2-\nu)}{2(1+\nu)}} \quad (3)$$

where $r_0 = 6$ mm denotes the initial radius for $p = 0$. As shown in Fig. 3(B), this analytical relationship agrees well with FEA, without any parameter fitting. FEA also shows that the $r \sim p$ curves in Fig. 3(B) are essentially the same for the balloon in the presence and absence of integrated electronics, suggesting that the electrodes and short serpentine interconnects have a negligible effect on balloon expansion in the circumferential direction. Therefore, the relationship in Eq. (3) strikingly holds for the balloon with electronics, due large part to the spring-like mechanical properties of the electronics.

Substituting Eq. (3) into the ratio expression in Eq. (2) gives an estimate of the length of the deformed balloon:

$$\frac{l}{l_0} = \left(\frac{r}{r_0} \right)^{\frac{1-2\nu}{2-\nu}} = \left[1 - \frac{(1 + \nu) r_0}{Eh_0} p \right]^{\frac{-(1-2\nu)}{2(1+\nu)}} \quad (4)$$

According to the modeling results in Fig. 3(C), this relationship is consistent with FEA for the bare balloon without applying any parameter fitting. However, both the analytical and FEA deviates significantly from the case where the balloon has integrated electronics. This is because the long serpentine interconnects along the axial direction significant increase tensile stiffness, thus inhibiting axial deformations. This effect can be observed by replacing tensile stiffness Eh in the third equation of Eq. (2) with the effective tensile stiffness $Eh + [EA / (2\pi r)]$, where EA

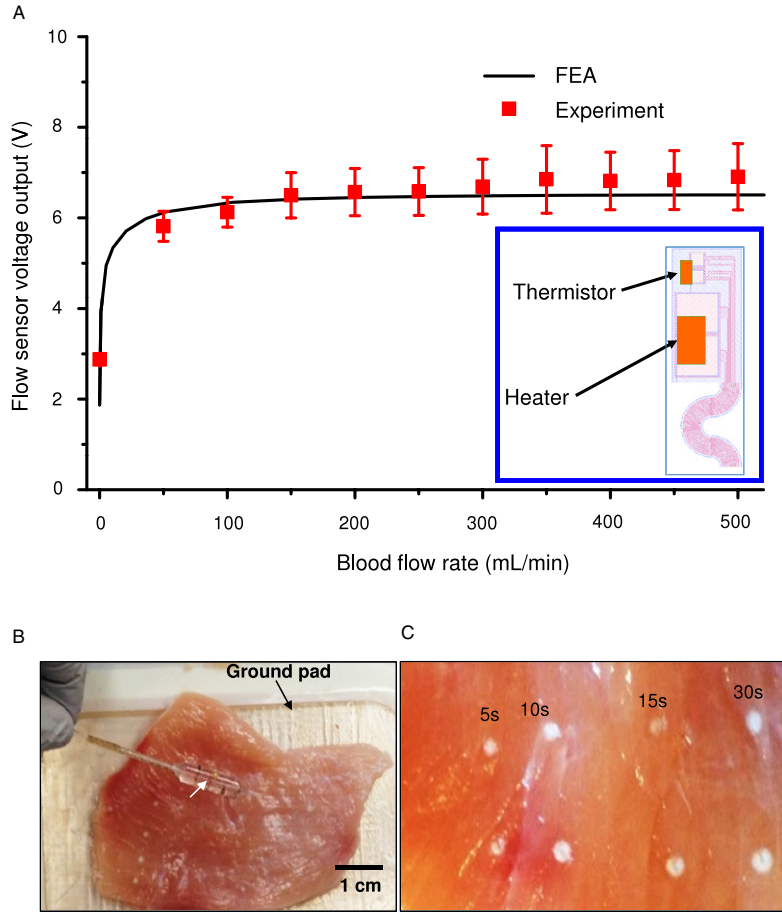


Fig. 4. Experimental results and thermal modeling of flow sensor and ablation bench-top studies. (A) Flow sensor voltage response as a function of volumetric flow in a perfusion chamber. (B) The modeling results based on feedback between the thermistor and heater, which are both controlled by a PID controller. (C) (Left panel) Balloon catheter with integrated stretchable electrodes pressed against chicken breast. Grounding pad resides underneath the chicken breast. Radio frequency energy is delivered through the electrodes and ground pad using unipolar configuration. (Right panel) The depth and areal coverage of the lesions were tested as a function of ablation duration.

is the effective tensile stiffness of the long serpentine interconnect and given as 35 N (when the strain approaches zero), where the long interconnect (5 μm -thick Au sandwiched between two 25 μm -thick PI) is modeled as curved beam with radius 0.67 mm, width 0.72 mm and the fan angle is 120° . The length of deformed balloon is then given by:

$$\frac{l}{l_0} = \sqrt{\frac{1 + \frac{2\pi E h_0 r_0}{EA} \left[1 - \frac{(1+\nu)r_0}{E h_0} p \right]^{\frac{-(1-2\nu)}{(1+\nu)}}}{1 + \frac{2\pi E h_0 r_0}{EA}}}, \quad (5)$$

which agrees reasonably well with FEA for the balloon with electronics subjected to $p < 0.4$ atm (Fig. 3(C)). The agreement is not as good for $p > 0.4$ atm because the long, serpentine interconnects buckle, as observed with FEA but this behavior is not accounted for in Eq. (5). Comparison of Fig. 3(C) and (B) clearly shows that the axial stretch l/l_0 is much smaller than the stretch r/r_0 in the circumferential direction.

3.2. Thermal properties of flexible flow sensor

In addition to characterizing the stretchable electrodes, we also account for the mechanical and thermal properties of the flexible flow sensor near the distal tip of the balloon catheter. According to this analysis, the flow sensor at the distal tip of the balloon is assumed to be largely isolated from both axial and circumferential strains. The geometry and layout of the thermistor relative to the heater are tuned to allow precise mapping of blood flow over the electrical current and near the temperature ranges employed in this study. Changes in local temperature distribution caused by changes in flow velocity serve as the mechanism by which blood velocity and volumetric flow rate are assessed [27,28]. During sensor operation, electrical current passes through the heater and thermistor. Once blood flow increases, the heat is carried downstream, creating a temperature difference between local blood and thermistor. This change in temperature is detected by the thermistor and, through a feedback loop, causes an increase in the heater's response output voltage in order to

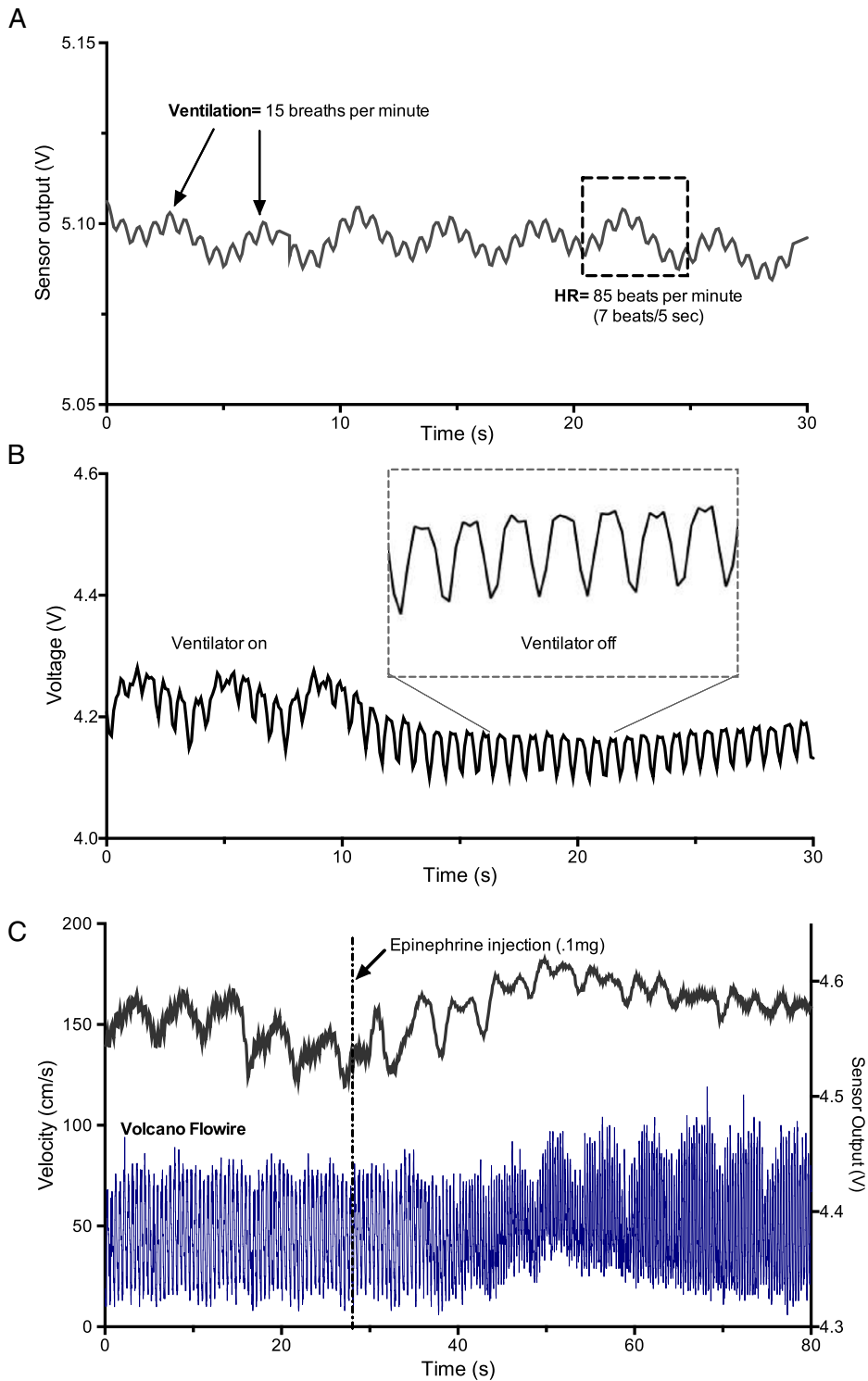


Fig. 5. In vivo analysis of blood flow during normal physiological function and drug injection. (A) Flow sensor measurements collected from within the renal artery in a healthy swine. The low frequency and high frequency patterns observed in the waveform correspond to breathing and heart rate, respectively. (B) Plot shows that turning off the ventilator caused the low frequency patterns (breathing patterns) to disappear, while the high frequency patterns (heart rate) were preserved. (C) Control studies to test the sensitivity and time response of the flow sensor. Injection of pharmacological agent (epinephrine) caused a transient rise in blood velocity, measured with the flow sensor and concurrently confirmed with a separate control device (Volcano FloWire).

maintain a constant temperature difference. FEA (e.g., FLU-ENT [29]) is used to study this process, where all the dimensions of the flow sensor and the diameter 4.7 mm of the artery are taken from the experiments. The thermal conductivity, density, and specific heat of blood are obtained from the literature as 0.5 W K m [30], 1069 kg/m³ and 3659 J/K kg [31], respectively. Fig. 4(A) shows the output voltage of the heater versus the blood flow rate obtained by FEA, which agrees very well with the experiments over a broad range of blood flow rate without any parameter fitting. The heater is no longer able to maintain a temperature differential in the surrounding blood once the flow rate reaches a threshold of 200 mL/min, as evidenced by asymptotic behavior in the flow sensor response at high flow profiles (Fig. 4(A)). The measurable range of the sensor is largely determined by the thermal properties of encapsulation material surrounding the material, and by the settings of the PID controller. The electrical current settings were set to match the flow rates in a porcine renal artery (100–200 mL/min), and could be adjusted to match the flow rates observed in human renal (200–300 mL/min) and peripheral arteries [32,33].

3.3. Characterization of balloon electrode ablation in vitro

We tested the ability of the electrodes to stimulate, ablate and sense contact by monitoring electrical impedance at the tissue interface. Fig. 4(B), (C) shows multiple lesions formed on chicken breast by applying RF energy through the balloon electrodes in unipolar configuration, with a ground electrode pad placed underneath the tissue substrate. Tissue contact was assessed according to changes in electrical impedance measured between individual sensor and a fixed ground within the backend circuitry of the catheter. The balloon is inflated with cold saline, which helps to cool the electrodes during ablation cycles and reduce the likelihood of charring. The transmural lesions generated by the balloon electrodes extended 4–6 mm deep in response to 1–2 W applied, with no evidence of charring. The flow sensor at the distal tip of the balloon can be used in conjunction with the balloon electrodes to verify tissue contact or vessel occlusion for electrical sensing and/or ablation by detecting a reduction in blood flow. These functionalities are critical for minimally invasive ablation or electroceutical procedures that require electrical stimulation coupled with hemodynamic monitoring to ensure intra-procedural safety and the delivery of adequate therapy.

3.4. In vivo blood flow sensing using flexible flow sensor

In vivo animal studies in which the catheter is routed into the renal artery highlight the utility of the flow sensor to capture a variety of physiological responses. Fig. 5(A) shows the flow sensor is sufficiently sensitive with rapid response time to capture low frequency breathing patterns (~15 breaths/min) and high frequency pulsatile waveforms due to the heartbeat (~85 beats/min) when the catheter is placed at the renal artery. In Fig. 5(B), we show that by turning off the mechanical ventilator, the low frequency breathing waveforms disappear, without

disturbance of the higher frequency pulsatile waveforms. The ability to detect these breathing patterns could prove valuable for intraprocedural respiratory monitoring in a clinical setting, when a patient is not being ventilated mechanically. Finally, we test the response of the flow sensor in response to the administration of pharmacological agents and use a commercially available blood flow monitoring system (Volcano FloWire catheter) to baseline the measurements (Fig. 5(C)). Injection of epinephrine caused a transient increase in blood flow, as captured by the flow sensor and concurrently verified with the Volcano FloWire. The ability of this flow sensor to detect pharmacological responses further demonstrates its potential utility in a clinical setting.

4. Conclusions

The mechanics and fabrication strategies presented in this study highlight recent advances leading to a new class of angioplasty balloon catheters with integrated blood flow, ablation, electrical contact, and mechanical contact sensing functionalities. These sensors and actuators are fabricated in ultrathin stretchable formats that enable minimal mechanical loading on the balloon substrate. As a result, these next generation balloon-based catheter systems provide intraprocedural feedback in real time, thus enabling faster procedure times, fewer instruments, and higher efficacy for vascular interventions.

Competing financial interests The authors declare no competing financial interest.

Acknowledgments

We thank Louis-Georges Guy, Diane Beaudry, Martin Laflamme, Pascal St-Jacques, and the rest of the AccellAB staff for their assistance during this study. Y. Huang acknowledges the National Institutes of Health under award number [R01EB019337].

References

- [1] M.J. Slepian, R. Ghaffari, J.A. Rogers, Multifunctional balloon catheters of the future, *Interv. Cardiol.* 3 (2011) 417–419.
- [2] U. Sigwart, J. Puel, V. Mirkovich, F. Joffre, L. Kappenburg, N. Engl. J. Med. 316 (1987) 701–706.
- [3] G.G. Stefanini, D.R. Holmes, Drug-eluting coronary-artery stents, *N. Engl. J. Med.* 368 (2013) 254–265.
- [4] C. Stettler, et al., Outcomes associated with drug-eluting and bare-metal stents: a collaborative network meta-analysis, *Lancet* 370 (2007) 937–948.
- [5] B.M. Hawkins, T.A. Henneby, Local paclitaxel delivery for treatment of peripheral arterial disease, *Circulation* 4 (2011) 297–302.
- [6] J.F. Viles-Gonzalez, F. Valentin, J.J. Badimon, Atherothrombosis: a widespread disease with unpredictable and life-threatening consequences, *Eur. Heart J.* 25 (2004) 1197–1207.
- [7] C.L. De Korte, J.A. Schaar, F. Mastik, P.W. Serruys, A.F.W. Van der Steen, Intravascular elastography: from bench to bedside, *J. Interv. Cardiol.* 16 (2003) 253–259.
- [8] G. Guagliumi, V. Sirbu, Optical coherence tomography: high resolution intravascular imaging to evaluate vascular healing after coronary stenting, *Catheter. Cardiovasc. Interv.* 72 (2008) 237–247.
- [9] J.A. Ormiston, et al., Renal denervation for resistant hypertension using an irrigated radiofrequency balloon: 12-month results from the Renal Hypertension Ablation System (RHAS) trial, *EuroPCR* 9 (2013) 70–74.

- [10] P. Schauerte, et al., Catheter ablation of cardiac autonomic nerves for prevention of vagal atrial fibrillation, *Circulation* 102 (2000) 2774–2780.
- [11] H.J. Chung, et al., Stretchable, multiplexed pH sensors with demonstrations on rabbit and human hearts undergoing ischemic, *Adv. Healthc. Mater.* 3 (2014) 59–68.
- [12] D.H. Kim, et al., Materials for multifunctional balloon catheters with capabilities in cardiac electrophysiological mapping and ablation therapy, *Nat. Mater.* 10 (2011) 316–323.
- [13] D.H. Kim, N. Lu, R. Ghaffari, J.A. Rogers, Inorganic semiconductor nanomaterials for flexible and stretchable biointegrated electronics, *NPG Asia Mater.* 4 (2012) e15. <http://dx.doi.org/10.1038/am.2012.27>.
- [14] D.H. Kim, R. Ghaffari, N. Lu, J.A. Rogers, Flexible and stretchable electronics for biointegrated devices, *Annu. Rev. Biomed. Eng.* 14 (2012) 113–128.
- [15] J. Viventi, et al., Flexible, foldable, actively multiplexed, high-density electrode array for mapping brain activity *in vivo*, *Nat. Neurosci.* 14 (2011) 1599–1605.
- [16] J. Dewire, H. Calkins, State-of-the-art and emerging technologies for atrial fibrillation ablation, *Nat. Rev. Cardiol.* 7 (2010) 129–138.
- [17] J.D. Burkhardt, A. Natale, New technologies in atrial fibrillation ablation, *Circulation* 120 (2009) 1533–1541.
- [18] S.P. Lacour, et al., Flexible and stretchable micro-electrodes for *in vitro* and *in vivo* neural interfaces, *Med. Biol. Eng. Comput.* 48 (2010) 945–954.
- [19] T. Someya, et al., Conformable, flexible, large-area networks of pressure and thermal sensors with organic transistor active matrixes, *Proc. Natl. Acad. Sci. USA* 102 (2005) 12321–12325.
- [20] T. Sekitani, et al., Organic nonvolatile memory transistors for flexible sensor arrays, *Science* 326 (2009) 1516–1519.
- [21] D. Son, et al., Multifunctional wearable devices for diagnosis and therapy of movement disorders, *Nat. Nanotechnol.* 9 (2014) 397–404.
- [22] J.A. Fan, et al., Fractal design concepts for stretchable electronics, *Nat. Commun.* 5 (2014) 3266.
- [23] M.E. Spira, A. Hai, Multi-electrode array technologies for neuroscience and cardiology, *Nat. Nanotechnol.* 8 (2013) 83–94.
- [24] ABAQUS. Analysis user's manual v.6.9. Pawtucket, RI: Dassault Systèmes, 2009.
- [25] D.H. Kim, et al., Electronic sensor and actuator webs for large-area complex geometry cardiac mapping and therapy, *Proc. Natl. Acad. Sci. USA* 109 (2012) 19910–19915.
- [26] H. Hocheng, C.M. Chen, Design, fabrication and failure analysis of stretchable electrical routings, *Sensors* 14 (2014) 11855–11877.
- [27] N.T. Nguyen, Micromachined flow sensors—a review, *Flow Meas. Instrum.* 8 (1997) 7–16.
- [28] R.M. Nerem, et al., Hot-film anemometer velocity measurements of arterial blood flow in horses, *Circ. Res.* 34 (1974) 193–203.
- [29] I.N.C. Fluent, FLUENT 6.3 user's guide. Fluent documentation, 2006.
- [30] R.C. Webb, et al., Ultrathin conformal devices for precise and continuous thermal characterization of human skin, *Nature Mater.* 12 (2013) 938–944.
- [31] J. Koo, C. Kleinstreuer, A new thermal conductivity model for nanofluids, *J. Nanopart. Res.* 6 (2004) 577–588.
- [32] M. Möckel, et al., Continuous measurements of renal perfusion in pigs by means of intravascular Doppler, *Kidney Int.* 59 (2001) 1439–1447.
- [33] S.O. Oktar, et al., Blood-flow volume quantification in internal carotid and vertebral arteries: comparison of 3 different ultrasound techniques with phase-contrast MR imaging, *Am. J. Neuroradiol.* 27 (2006) 363–369.